AIAA 98–0712

Reduction and Analysis of Phosphor Thermography Data With the IHEAT Software Package

N. Ronald Merski

NASA Langley Research Center, Hampton, VA 23681

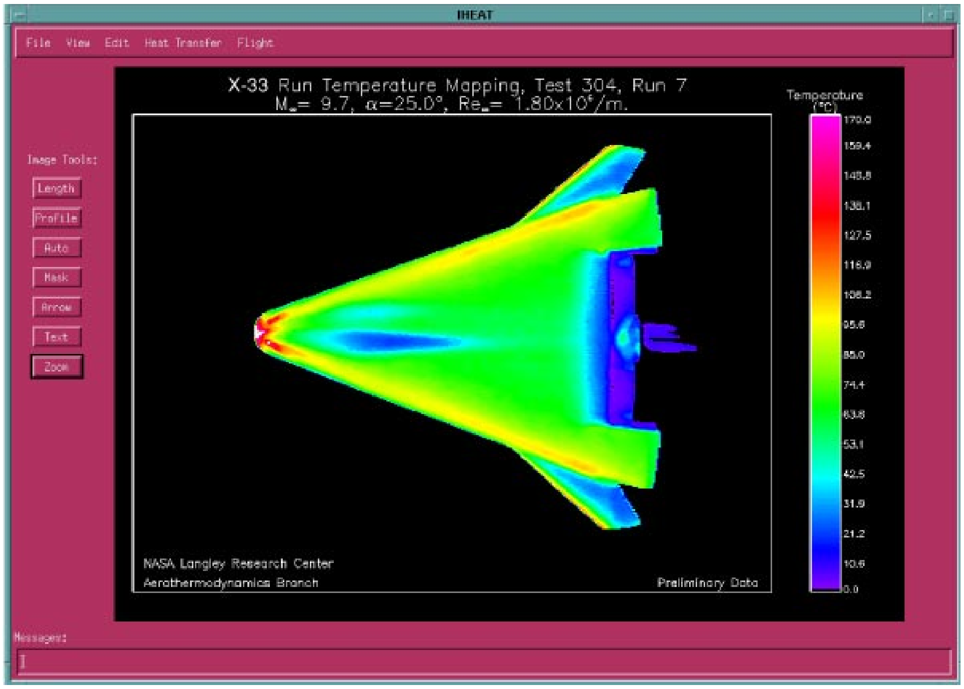

36th AIAA Aerospace Sciences Meeting and Exhibit
January 12–15, 1998/Reno, NV

Reduction and Analysis of Phosphor Thermography Data With the IHEAT Software Package

N. Ronald Merski*
NASA Langley Research Center, Hampton, VA 23681

Detailed aeroheating information is critical to the successful design of a thermal protection system (TPS) for an aerospace vehicle. This report describes NASA Langley Research Center's (LaRC) two-color relative-intensity phosphor thermography method and the IHEAT software package which is used for the efficient data reduction and analysis of the phosphor image data. Development of theory is provided for a new weighted two-color relative-intensity fluorescence theory for quantitatively determining surface temperatures on hypersonic wind tunnel models; an improved application of the one-dimensional conduction theory for use in determining global heating mappings; and extrapolation of wind tunnel data to flight surface temperatures. The phosphor methodology at LaRC is presented including descriptions of phosphor model fabrication, test facilities and phosphor video acquisition systems. A discussion of the calibration procedures, data reduction and data analysis is given. Estimates of the total uncertainties (with a 95% confidence level) associated with the phosphor technique are shown to be approximately 8 to 10 percent in the Langley's 31-Inch Mach 10 Tunnel and 7 to 10 percent in the 20-Inch Mach 6 Tunnel. A comparison with thin-film measurents using two-inch radius hemispheres shows the phosphor data to be within 7 percent of thin-film measurements and to agree even better with predictions via a LATCH computational fluid dynamics solution (CFD). Good agreement between phosphor data and LAURA CFD computations on the forebody of a vertical takeoff/vertical lander configuration at four angles of attack is also shown. In addition, a comparison is given between Mach 6 phosphor data and laminar and turbulent solutions generated using the LAURA, GASP and LATCH CFD codes. Finally, the extrapolation method developed in this report is applied to the X-34 configuration with good agreement between the phosphor extrapolation and LAURA flight surface temperature predictions. The phosphor process outlined in the paper is believed to provide the aerothermodynamic community with a valuable capability for rapidly obtaining (4 to 5 weeks) detailed heating information needed in TPS design.

Nomenclature

A	Extrapolation factor constant
C	Heat transfer coefficient constant, $= h(i_w/Tw)$
D	Driver constant, $= i_{aw}(T_w/i_w) - T_{init}$
F	Flux of light, power/unit area
H	Ratio of local heat transfer coefficient and stagnation point heat transfer coefficient
I	Intensity, projected radiant power into solid angle
K	Coating coefficient
L	Configuration length
M	Mach number
Pr	Prandtl number
Q	Radiant Power
R	Sphere radius
Re	Reynolds number
T	Temperature
V	Velocity
X	Extrapolation coefficient
a	Effective aperture factor of camera optics
b	Vehicle wing span from wing tip to wing tip
c	Specific heat of model substrate
h	Heat transfer coefficient
i	Enthalpy
j	Fluorescent light per unit path length
k	Thermal conductivity of model substrate
$\dot{q}$	Heat transfer rate per unit area
r	Recovery factor
t	Time
x	Axial location on configuration, nose is x=0
y	Spanwise location
z	Distance into substrate
Δ	Weighted logarithmic difference
Λ	Variable from Laplace Transform,$= C\sqrt{t}/\beta$
$\Phi(T)$	Temperature dependent fluorescence factor
α	Vehicle angle of attack
β	Thermal product, $= \sqrt{\rho c k}$

---

*Aerospace Technologist, Aerothermodynamics Branch, Aero- and Gas-Dynamics Division, Research and Technology Group, Senior Member AIAA.

γ	Ratio of specific heats
δ	Elemental area
ϵ	Surface emissivity
η	Ratio of fluorscence exponents, ν_r and ν_g
θ	Temperature minus initial temperature
κ	Thermal diffusivity, $= k/\rho c$
ν	Fluorscence exponent
ξ	Running length along configuration
ρ	Density
σ	Stefan-Boltzmann constant
τ	Window transmissivity

Subscripts

FL	Flight conditions
G	Green component fluorescent light
R	Red component fluorescent light
UV	Ultraviolet portion of spectrum
WT	Wind tunnel conditions
aw	Adiabatic wall conditions
$conv$	Convective
e	Boundary layer edge conditions
eff	Effective
gaw	Global adiabatic wall value
$init$	Initial conditions
lam	Laminar boundary layer state
$lamp$	UV lamp
rad	Radiative
run	Wind tunnel run data reduction time
st	Stagnation point
tl	Total conditions
tur	Turbulent boundary layer state
w	Conditions at the model surface
λ	Wavelength of light
∞	Freestream

Introduction

A number of U.S. hypersonic vehicle initiatives have occurred over the last few years. For most of these programs, the experimental aeroheating data used for design of the thermal protection systems (TPS) and establishment of TPS flight margins has been obtained (often exclusively) with the phosphor thermography method. The IHEAT phosphor imaging software package was used for the data reduction. This phosphor thermography approach along with the efficient data reduction by the IHEAT software is revolutionary. Vehicle designers can obtain detailed global, quantitative, parametric heating data within a month after a request. Recent applications of phosphor thermography and IHEAT include code comparison and cross-flow transition studies on the McDonnell Douglas Delta Clipper Vertical-Takeoff/Vertical-Lander configuration, a shuttle orbiter boundary layer transition roughness study,[1] parametric full configuration studies in support of Lockheed, Rockwell, and McDonnell Douglas X-33 Phase 1 concepts, full configuration heating studies on the the X-33 Phase 2 concept[2,3] and on the X-34 vehicle,[4] full configuration heating on the X-38[5–7] and base heating for the Mars Microprobe project.

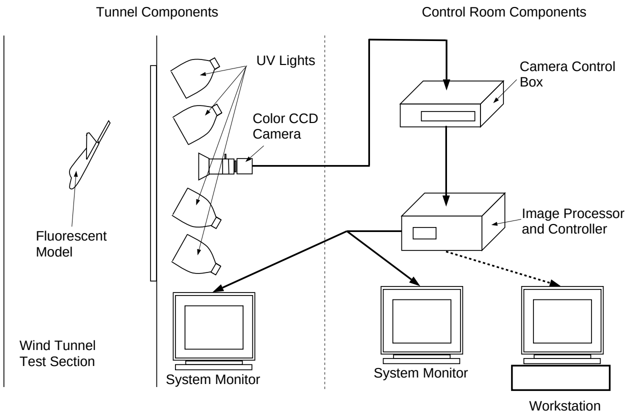

Fig. 1 Phosphor test setup.

Early development of NASA Langley's two-color relative-intensity phosphor thermography technique is described in Refs. 8–10. With this method, ceramic wind tunnel models are fabricated and coated with phosphors which fluoresce in two regions of the visible spectrum when illuminated with ultraviolet light. One of the phosphors ($ZnCdS : Ag, Ni$) is a broadband thermographic phosphor fluorescing primarily in the green portion of the spectrum and the other is a narrowband rare-Earth ($La_2O_2S : 1\%Eu$) which has two green emission spikes and a red emission spike. The fluorescence intensity is dependent upon the amount of incident ultraviolet light and the phosphor temperature. By acquiring fluorescence intensity images with a color video camera of an illuminated phosphor model exposed to flow in a wind tunnel (see Fig. 1), surface temperature mappings are calculated on the portions of the model which are in the field of view of the camera. This is done by utilizing the green and red camera outputs and entering the resulting intensity images into lookup tables created during the calibration of the system. With the present phosphors, a usable temperature range of 70 to 340$^\circ F$ is obtained. In addition, using temperature images acquired at different times in a wind tunnel run, heat transfer images are computed immediately following a run using the one-dimensional heat conduction equation.

This report presents an overview of the NASA Langley phosphor thermography method and its implementation in the IHEAT data reduction and analysis software. It highlights doctoral work which will be published in greater detail in Ref. 11. First, a new weighted two-color relative-intensity phosphor thermography theory will be introduced which enables a greater degree of accuracy in high-temperature global phosphor thermography measurements. In addition, an improved application of the one-dimensional heat conduction equation will be presented which increases the accuracy of global heating data. Proposed factors for extrapolating wind tunnel heating data to flight surface temperatures are also developed. Next, an overview of the phosphor thermography procedure at the Langley Research Center will be provided along with a description of the individual components of the IHEAT software package. Then, comparisons of phosphor heating data to thin-film measurements and predictions from the LAURA, GASP and LATCH CFD codes will be presented. Finally an application of the extrapolation method to X-34 laminar and turbulent flight conditions will be given.

Theory

Weighted Two-Color Relative-Intensity Fluorescence Theory

This section develops a weighted two-color relative-intensity theory for quantitatively determining temperature from measurement of fluorescent light emitted by a model's phosphor coating. In analyzing this problem, light from UV lamps illuminates the phosphor coating, the phosphor coating then emits visible light which travels through a wind tunnel window into the optics of a video camera and finally to a Charge Coupled Device (CCD) array. Ultimately, there are two primary unknown variables – the local surface temperature and the local illumination of UV light on the model. A number of other factors (including model coating characteristics, facility window transmissivity, and optical response among others), however, must be accounted for or be kept constant from the calibration process to the final data reduction.

The flux of UV light which excites the phosphor is equal to the flux of UV light from the lamps times a coating factor.

$$F_{UV} = K_{UV} F_{lamp} \tag{1}$$

The coating factor, K_{UV}, is dependent on the absorption rate of the phosphor coating, the coating thickness, surface reflectivity of the model surface, and incident angle of UV light on a model. A detailed understanding of the dependency of the coating factor on these variables can be obtained by using the Radiative Transfer Equation.[11]

The resulting emission response of the phosphors from the UV illumination is not necessarily linearly proportional to the amount of UV light incident on the model. Thus, unless the fluorescence characteristics are the same for two spectral bands or at two different temperatures, a straight ratio cannot be used to remove dependence on UV illumination as is often done for relative-intensity approaches. This is particularly true when phosphors are mixed which have different response characteristics to UV light. Not accounting for these fluorescence response charateristics can affect measurements on wind tunnel models having local UV light illumination levels which significantly deviate from intensities used during calibration, particularly on configurations with large amounts of surface curvature. This nonlinearity is caused by the phosphor approaching a saturation limit in regards to excitation. Reference 12 describes a number of possible curve-fits for the nonlinear response, the simplest of which is a power curve. The intensity of fluorescent light per unit path length emitted by a phosphor illuminated with UV light, j_λ, can therefore be described as:

$$j_\lambda = \Phi_\lambda(T) F_{UV}^{\nu_\lambda(T)} \tag{2}$$

All parameters in Equation 2 are dependent upon the region of the emission spectrum being modelled and this is denoted by the subscript λ.

The intensity of light from the surface of the model can be expressed as the fluorescent power per unit path length times a coating function:

$$I_\lambda = j_\lambda K_\lambda \tag{3}$$

Once the fluorescent phosphor light is emitted from the model surface, it passes through the tunnel window to the camera optics and reaches the camera CCD array. The radiant power of light which is incident on the CCD array can be expressed as:

$$\delta Q = \tau_w a I \tag{4}$$

where τ is the window transmissivity and a is an effective aperture factor which accounts for the transmission of light through the camera optics.

Substitution of Equations 1 through 3 into Equation 4 yields

$$\delta Q_\lambda = \tau_{w,\lambda} a_\lambda K_\lambda \Phi_\lambda(T) \left[K_{UV} F_{lamp}\right]^{\nu_\lambda(T)} \tag{5}$$

Equation 5 primarily depends on the amount of incident UV light on the model and the local temperature of the phosphor coating. To extract temperature from this equation, the dependence on UV light must be eliminated. This is where the relative-intensity method comes in. By analyzing the fluorescence from the model within two different regions of the spectrum, two equations with two unknowns exist and the UV light dependence can be removed. To do this, the natural logarithm is taken of Equation 5 for two color components (in this case red and green):

$$ln(\delta Q_R) = ln\left[\tau_{w,R} a K_R \Phi_R(T)\right] + \nu_R(T) ln\left[K_{UV} F_{lamp}\right] \tag{6}$$

$$ln(\delta Q_G) = ln\left[\tau_{w,G} a K_G \Phi_G(T)\right] + \nu_G(T) ln\left[K_{UV} F_{lamp}\right] \tag{7}$$

At this point, a ratio of the fluorescence powers, η is defined:

$$\eta = \frac{\nu_R}{\nu_G} \tag{8}$$

Multiplying Equation 7 by 8 and subtracting the result from 6 causes the UV dependence to drop out and yields the weighted two-color relative-intensity equation:

$$ln(\delta Q_R) - \eta(T) ln(\delta Q_G) = \Delta(T) \tag{9}$$

where Δ is defined as the *weighted logarithmic difference* and is given by:

$$\Delta(T) = ln\left[\tau_{w,R} a K_R \Phi_R(T)\right] - \eta(T) ln\left[\tau_{w,G} a K_G \Phi_G(T)\right] \tag{10}$$

In order to determine the temperature from Equation 9, Δ and η as a function of temperature must be calibrated. Then given incident amounts of green and red light on the camera array a Δ value is formed and an iteration has to be performed to back out the temperature.

Heat Transfer Theory

This section describes the theory used in the reduction of the phosphor thermography data to heat transfer mappings. In reducing the phosphor data, the phosphor coating is assumed to be infinitely thin, the convective heat transfer is assumed to be transmitted normally into the model surface and the local surface radius of curvature is assumed to be large. The one-dimensional heat conduction equation can therefore be solved which greatly simplifies the data reduction. The one-dimensional approach has its limitations, but for insulative ceramics such as fused silica and for short test times of less than a second, the approximation works well. In the development of the present heat transfer theory, the thermal properties of the fused silica will be assumed to not be dependent on temperature. A simple correction to account for this assumption will be described at the end of the section.

The governing one-dimensional heat conduction equation is given by:

$$\rho c \frac{\partial \theta}{\partial t} = \frac{\partial}{\partial z}\left(k \frac{\partial \theta}{\partial z}\right) \tag{11}$$

Assuming the thermal properties of the substrate material to not be dependent on temperature, Equation 11 becomes:

$$\frac{\partial \theta}{\partial t} = \kappa \frac{\partial^2 \theta}{\partial z^2} \tag{12}$$

where $\kappa = k/\rho c$ is the thermal diffusivity of the substrate material.

In order to solve Equation 12, one initial condition and two boundary conditions are required. For an initial condition, the temperature in a direction normal to the surface at a given location is assumed to be constant before the injection of the model in the wind tunnel:

$$\theta(z, 0) = 0 \tag{13}$$

For one of the boundary conditions, an infinite slab assumption is made whereby the temperature at some location into the model is always equal to the initial temperature:

$$\theta(\infty, t) = 0 \tag{14}$$

For the second boundary condition, the normal conduction into the wind tunnel model is set equal to the convective surface heating:

$$-k \frac{\partial \theta}{\partial z} \mid_{z=0} = \dot{q}_{conv} \tag{15}$$

where $\dot{q}_{conv}$ is the convective heat transfer rate per unit area.

The convective heating boundary condition is further assumed to experience a jump to a constant heat transfer coefficient during the injection of a model into a wind tunnel. Typically, for development of similar data reduction approaches, the convective definition is temperature based, however, this assumption is strictly true only for a calorically perfect gas (constant specific heat). In the case of the hypersonic facilities at Langley, the reservoir temperature is past the limits of a calorically perfect gas and an error can occur when using the temperature-based approach. Therefore an enthalpy-based definition is used where:

$$\dot{q}_{conv} = h(i_{aw} - i_w) \tag{16}$$

In order to solve the conduction equation using Laplace transforms, the convective condition needs to be rewritten in terms of temperature. Pulling out a ratio of the surface enthalpy to surface temperature, Equation 16 can be rewritten as:

$$\dot{q}_{conv} = h\left(\frac{i_w}{T_w}\right)\left[\left(\frac{T_w}{i_w}\right) i_{aw} - T_w\right] \tag{17}$$

For the temperature range over which the phosphor coating can detect, the air is calorically perfect so the ratio of the surface enthalpy to the surface temperature is nearly constant and the convection definition is now in a form which can be used with Laplace transforms.

Substituting Equation 17 into Equation 15 the surface boundary condition becomes:

$$-k \frac{\partial \theta}{\partial z} \mid_{z=0} = C(D - \theta_w) \tag{18}$$

where C and D are constants equal to $h(i_w/T_w)$ and $i_{aw}(T_w/i_w) - T_{init}$ respectively.

Equation 12 can now be solved with Laplace transforms using conditions given by Equations 13,14 and 18. At the surface of the model, the solution is given by:

$$\frac{\theta_w}{D} = 1 - e^{\Lambda^2} erfc\ \Lambda \tag{19}$$

where $\Lambda = C\sqrt{t}/\beta$. This equation (which will be referred to as the step equation) is used for reducing the phosphor data.

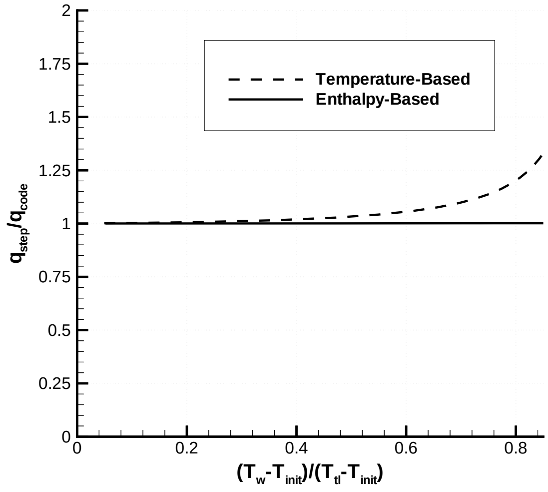

Fig. 2 Comparison of heat transfer rate computation between enthalpy-based and temperature-based methods.

Only an initial temperature and a temperature at some time into a tunnel run is required to solve the equation. Thus, in a wind tunnel run, an initial temperature image can be acquired before a run with no flow on the model and then a temperature image can be obtained during a run and Equation 19 can be solved at each pixel in the image. No temperature time history is needed which is important with an imaging method because temperature histories of images would require a large amount of computer storage space.

The effect of using an enthalpy-based approach versus the conventional temperature-based approach is seen in Figure 2. In creating the figure, a conduction code was run with a constant heat transfer coefficient as the surface boundary condition and heat transfer rates were computed with both approaches using the solution's surface temperature value. The computed heat transfer rates were nondimensionalized with the heat transfer rate from the conduction solution. The resulting heat transfer ratios are plotted versus a temperature difference ratio, $(T_w - T_{init})/(T_{tl} - T_{init})$. From the figure it can be seen that as the wall temperature approaches the tunnel total temperature, the error with the temperature-based method begins to climb rapidly, while the enthalpy-based method remains constant.

In reality, the time, t, in Equation 19, does not start from the moment the model begins to heat. As the model travels through the test section wall boundary layer it does not experience a step in the heat transfer coefficient as was assumed in the heat transfer theory. Therefore, the injection process is modelled as a step in heating with the step in the heat transfer coefficient occurring at some time as the model passes through the boundary layer. The effective time at which the step occurs can be calibrated by acquiring data with a discrete gauge model. The heat transfer rate computed using a time-history based method can then be put into Equation 19 and a time backed out. Typical variations of the effective time on a model are between 1 and 2 percent. After performing a number of these "calibrations," a simple approximation for determining the effective time has been observed:

$$t_{eff} = t_{run} - t_{wall} - (t_{wall} - t_{bl}) \times 0.5 \tag{20}$$

where t_{run} is the run time at which the data was acquired and t_{bl} is the time that the model reaches the edge of the tunnel boundary layer as determined from tunnel calibrations. This method of determining the effective time is currently the preferred approach. Effectively it exchanges possible inconsistencies in the injection hydraulics with inconsistencies in the tunnel calibration profile.

The thermal product, β, in Equation 19 is determined from a combination of thermal conductivity and thermal diffusivity measurements from the equation:

$$\beta = \frac{k}{\sqrt{\kappa}} \tag{21}$$

For fused silica, samples have been tested at Anter Laboratories, Inc., of Pittsburgh, PA, to determine tehermal properties and curve-fits have been computed from the resulting data:

$$\begin{aligned}\kappa = \; & 9.212605264 \times 10^{-6} - 1.91963306 \times 10^{-9} T \\ & + 1.79201 \times 10^{-12} T^2 \; \tfrac{m^2}{s}\end{aligned} \tag{22}$$

$$k = 0.668170765 - 0.000681630 \times T \; \frac{W}{m-K} \tag{23}$$

Up to this point, the heat transfer analysis has assumed that the thermal properties, k, κ, and β are constant with respect to temperature although this is not true. If room temperature properties are assumed, as much as a 17% error can occur at the high end of the phosphor measurement range. For the phosphor thermography image data reduction, a relatively straight-forward approach is proposed for correcting the variable properties effects. The thermal product at the initial room temperature, β_{init}, is averaged with the thermal product at the run temperature, β_{run}, to give an effective thermal product, β_{eff}, used for data reduction. Thus,

$$\beta_{eff} = \frac{\beta_{init} + \beta_{run}}{2} \tag{24}$$

To check this equation, a one-dimensional infinite slab conduction code was run in a variable property mode for a range of heat transfer coefficients. The code was run for both fused silica and Macor thermal properties and resulting surface temperatures were reduced

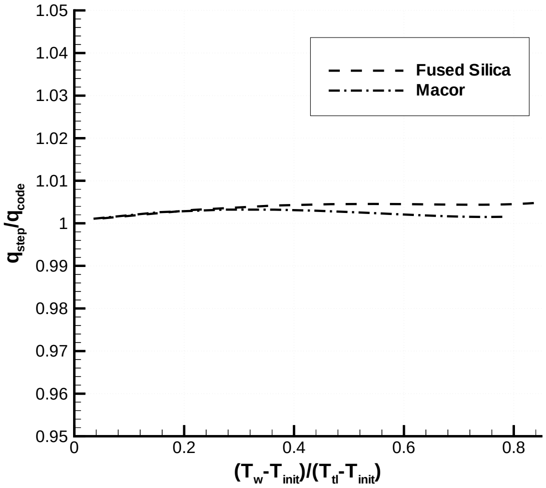

Fig. 3 Error of variable thermal properties approximation.

using Equation 19. The results are plotted in Figure 3. Here again, the ratio of reduced heat transfer rate to the heat transfer rate from the code, q_{step}/q_{code}, is plotted against the temperature difference ratio, $(T_w - T_{init})/(T_{tl} - T_{init})$. The heat transfer rates for both the corrected fused silica and the Macor are within 0.4% for the full range of temperature difference ratios. This error is less than the error associated with absolute values of the thermal properties, so Equation 24 is believed to be sufficient for data reduction with fused silica and Macor substrates.

In order to determine an adiabatic wall enthalpy,i_{aw}, the ratio of the adiabatic wall enthalpy to the total enthalpy can be found from the expression:

$$\frac{i_{aw}}{i_{tl}} = \frac{1 + r\frac{\gamma-1}{2}M_e^2}{1 + \frac{\gamma-1}{2}M_e^2} \tag{25}$$

For laminar flows, the recovery factor, r, is equal to $\sqrt{Pr}$ and for turbulent flow it is equal to $Pr^{1/3}$. The edge Mach number can be estimated by using tangent-wedge approximations with the oblique shock relations. Along the body, the adiabatic wall enthalpy decreases from the total enthalpy. Currently for the phosphor thermography method the local surface angle at a pixel is not known. So with laminar extrapolations, the strategy is to find the lowest adiabatic wall enthalpy on a configuration and then average this result with the total enthalpy to obtain a global adiabatic wall enthalpy. In the case of turbulent extrapolations where the flow trips back on the body, the adiabatic wall enthalpy is just selected as the adiabatic wall enthalpy on a wedge with an angle equal to the angle of attack of the vehicle.

Extrapolation of Phosphor Data To Flight Surface Temperatures

Once the heat transfer coefficient mappings have been determined via wind tunnel tests, they can be used to validate CFD predictions, to determine dispersion heating factors or to predict the surface temperature of a vehicle in flight. This last use for the data, extrapolation to flight, has the possibility of saving large amounts of computational time required for flight predictions. This section describes a method which has been developed for use with IHEAT phosphor images and has been successfully applied to the X-34 configuration.

A standard approach to extrapolationg wind tunnel aeroheating data to flight is to reference heat transfer coefficients on a scaled configuration in the wind tunnel to the heat transfer coefficient at the stagnation point on a reference hemisphere at the tunnel conditions. As described in Ref. 13, this ratio can then be related to the heat transfer coefficient for the full configuration in flight ratioed by the heat transfer coefficient of a scaled up reference hemisphere using the expression:

$$\frac{H_{FL}}{H_{WT}} = X \tag{26}$$

where the H's are the ratio of the local surface heat transfer coefficient divided by the stagnation point heat transfer coefficient on a sphere at flight or wind tunnel conditions and X is an extrapolation factor. The extrapolation factor adjusts the data for differences between wind tunnel and flight such as in Mach number, Reynolds number and the existence of turbulence.

Heat transfer rate correlations reported by Tauber and Meneses[14,15] were used as a guide in developing the form for the extrapolation factors. The local heat transfer coefficient at a sphere stagnation point is assumed to be approximated by:

$$h_{st} = \rho_\infty^{.5} V_\infty^3 \left(\frac{R}{L}\right)^{-.5} L^{-.5} \frac{A_{st}}{i_{tl}} \tag{27}$$

where R is the radius of the sphere, L is the length of the geometry and A is a constant dependent on angle of attack and geometry considerations. Likewise for a laminar flat plate:

$$h_{lam} = \rho_\infty^{.5} V_\infty^{3.2} \left(\frac{\xi}{L}\right)^{-.5} L^{-.5} \frac{A_{lam}}{i_{tl}} \tag{28}$$

where ξ is the running length from the start of a streamline. Finally in the case of turbulent heating on a flat plate:

$$h_{tur} = \rho_\infty^{.8} V_\infty^{3.7} \left(\frac{\xi}{L}\right)^{-.2} L^{-.2} {T_w}^{-.25} \frac{A_{tur}}{i_{tl}} \tag{29}$$

where ξ in this case is the running length from the start of transition.

Extrapolation factors for laminar and turbulent flows can now be determined by dividing the local laminar or turbulent h (Equations 28 and 29 respectively) by the stagnation point h (Equation 27). The resulting ratio at flight conditions is then divided by the ratio at wind tunnel conditions. After cancellations are made for the running lengths, ξ, and the constants, A, the following laminar factor results:

$$X_{lam} = \frac{H_{lam,FL}}{H_{lam,WT}} = \left(\frac{V_{\infty,FL}}{V_{\infty,WT}}\right)^{.2} \quad (30)$$

and in the case of turbulent flow

$$X_{tur} = \frac{H_{tur,FL}}{H_{tur,WT}} = \left(\frac{\rho_{\infty,FL}}{\rho_{\infty,WT}}\right)^{.3} \left(\frac{V_{\infty,FL}}{V_{\infty,WT}}\right)^{.37} \times \left(\frac{L_{FL}}{L_{WT}}\right)^{.3} \left(\frac{T_{w,FL}}{T_{w,WT}}\right)^{-.25} \quad (31)$$

The heating at a point on the flight configuration is then determined by calculating the stagnation point heat transfer coefficient at a point on the trajectory on a sphere at the flight scale. The ratio from the wind tunnel is multiplied by this flight stagnation point coefficient and the extrapolation factor, X, to yield the flight heat transfer coefficient. The heat transfer rate is determined by multiplying the heat transfer coefficient by the thermal driver, $(i_{aw} - i_w)$.

The wall temperature in flight is predicted by assuming that the radiative heat transfer rate at the surface of the flight vehicle,$\dot{q}_{rad}$, is equal to the convective heat transfer rate into the vehicle surface,$\dot{q}_{conv}$:

$$\dot{q}_{rad} = \dot{q}_{conv} \quad (32)$$

From the Stefan-Boltzmann law, the radiative heat transfer rate is related to the surface temperature, T_{FL}, by:

$$\dot{q}_{rad} = \epsilon \sigma T_{FL}^4 \quad (33)$$

where ϵ is the surface emissivity and σ is the Stefan-Boltzmann constant. Substituting Equation 33 and the definition of the heat transfer coefficient into Equation 32 yields:

$$\dot{q}_{rad} = \epsilon \sigma T_{FL}^4 = h_{FL}(i_{aw,FL} - i_{w,FL}) \quad (34)$$

Since the wall enthalpy is dependent on the surface temparature, Equation 34 must be solved iteratively. If the flight total enthalpy is high enough however, the wall enthalpy can often be assumed to be small as compared to the adiabatic wall enthalpy and Equation 34 becomes

$$\dot{q}_{rad} = \epsilon \sigma T_{FL}^4 = H_{FL}\ i_{aw,FL} \quad (35)$$

This "cold wall" assumption, when applicable, removes the need for the iteration associated with Equation 34 and greatly simplifies the computations required for global images.

The adiabatic wall enthalpy is a fraction of the total flight enthalpy. To calculate the total flight enthalpy, half the square of the velocity is added to the local ambient enthalpy:

$$i_{tl} = V_{\infty}^2/2 + i_{\infty} \quad (36)$$

The enthalpy at the wall is determined using the thermodynamic property curve-fits for individual species reported in Ref. 16. Knowing the species fractions of air at a temperature and altitude, the enthalpy can be calculated. For this analysis, sea-level volume fractions of N_2, O_2, and Ar as defined by the *U.S. Standard Atmosphere, 1976*[17] are used. Even though the number densities of these species drop as the altitude increases, the fractional volumes remain constant up to $282{,}000 ft.$ and so the same enthalpy formulation can be used up to this altitude. At higher altitudes though, monatomic oxygen becomes a significant component of the ambient air and the fractional volumes must then be computed for each altitude.

As the temperature increases to $3000°F$, the air is no longer thermally perfect. The oxygen begins to dissociate and the proportions of the constituents of the air changes. Properties for air under equilibrium conditions can be determined, but a pressure dependency arises in the computation of the enthalpy. For this global extrapolation method, the surface pressure is not known on the vehicle so the method is thus restricted to surface temperatures of less than $3000°F$ if a cold-wall assumption cannot be applied, although typically when these temperatures are reached the cold-wall assumption is valid.

Upon extrapolating to flight, the adiabatic wall enthalpy is chosen to be the same fraction of the total enthalpy as in the case of the tunnel conditions, thus providing a consistent convective heat transfer definition. There is still an error in the computed heat transfer rate, however, resulting from the deviation of the chosen global adiabatic wall value from the true adiabatic wall value (proof not shown) of

$$\frac{\dot{q}_{FL,gaw}}{\dot{q}_{FL,aw}} = \left(\frac{i_{aw,WT} - i_{w,WT}}{i_{gaw,WT} - i_{w,WT}}\right) \left(\frac{i_{gaw,FL} - i_{w,FL}}{i_{aw,FL} - i_{w,FL}}\right) \quad (37)$$

where the subscript, gaw, stands for the global adiabatic wall value chosen for the whole phosphor image.

Phosphor Thermography Method in Langley Facilities

Model Fabrication

Fabrication of wind tunnel models for phosphor testing is a critical component in the technique. In order to obtain accurate heat transfer data using the one-dimensional heat conduction equation, models need to be made of a material with a low thermal diffusivity and well-defined, uniform, isotropic thermal properties. Also, the models must be durable for repeated use in the wind tunnel and they should be subject to minimal deformation when thermally cycled. To meet these requirements, Langley has developed a unique, silica ceramic slip casting method.[18] Patterns for the models are typically made using a numerical cutting machine or with the stereo-lithography process. Using these patterns, investment molds are created. Ceramic slip is poured into the molds and after the ceramic sets, the investment molds crumble off leaving ceramic shells. These shells are next fired in a kiln and potted with support hardware. The slip casting method allows for the casting of relatively fine details as well as thin ceramic sections such as wings and fins. Model lengths are typically 10 to 14 inches; however, models up to 30 inches in length have been fabricated for testing at low angles of attack. In addition, the slip-casting method is a rapid process whereby, in three to four weeks, a full array of models can be fabricated, complete with various perturbations in a configuration such as nose radius changes and control surface deflections.

Once the models are fabricated, they must be coated with phosphor crystals. Currently, the phosphors are suspended in a silica ceramic binder and applied with an airbrush. Final coating thicknesses have been measured to be approximately .001 inches. The coating method which has been developed, produces robust coatings which do not require reapplication between runs, thereby significantly enhancing the efficiency of the phosphor technique.

Facilities

Langley's phosphor thermography method has been used in four of the facilites in NASA Langley's Aerothermodynamic Facilities Complex (AFC): the 31-Inch Mach 10 Air, 20-Inch Mach 6 Air, 20-Inch Mach 6 CF_4 and 15-Inch Mach 6 High Temperature Tunnels. A detailed description of these facilities is given by Micol.[19] This section briefly describes the first two facilities where the phosphor method has been primarily used to date.

The 31-Inch Mach 10 facility consists of high pressure air storage rated to a maximum pressure of 4400 psia, a 12.5 MW electrical bundle heater which heats the air to approximately 1850 $^\circ R$, a settling chamber, three-dimensional contoured nozzle, test section, adjustable second minimum, aftercooler, vacuum spheres and vacuum pumps. A 5-micron in-line filter, before the nozzle, removes particles from the air-flow which can damage the ceramic phosphor models. The nozzle itself has a 1.07-in. square beryllium copper throat and its exit height is 31 inches. The test section has a 30-inch by 17-inch tempered-glass window for illuminating and viewing the phosphor models. Wind tunnel models are protected from the flow as the tunnel comes to its operating condition by a door in the side-wall of the test section. After the operating condition is reached, the model is injected to the tunnel centerline in approximately 0.55 sec from the back side of the test section with a hydraulic injection system. Freestream Reynolds numbers obtained in this tunnel varying from 0.25 to $2.2\times10^6/ft$.

The 20-Inch Mach 6 Tunnel has a two-dimensional contoured nozzle, with the bottom and top walls being contoured and the side walls parallel. The test section size is 20.5 *in.* by 20 *in.* and has tempered glass windows on the top and two sides. Models are mounted on an injection system in a housing below the test section. During a run, the models can be injected in less than 0.5 *sec*. The tunnel has a range of operating reservoir pressures from 30 to 500 psia and reservoir temperatures of up to 1000 $^\circ R$. This corresponds to a freestream Reynolds number range of 0.5 to $9.0\times10^6/ft$.

Acquisition Systems

Four phosphor thermography video acquisition systems have been constructed for use in Langley's hypersonic facilities, two of which are currently operational and two which will be brought online in the near future. The systems are composed of a Sony XC007 video camera with a zoom lens and a PC computer equipped with a Matrox Meteor digitizer. The Sony XC007 camera has 3 CCD arrays which obtain red, green and blue component images (only red and green being used for phosphor thermography). Each array has 768 horizontal picture elements and 493 vertical picture elements. Signal from the color CCD arrays travels into a camera control box which performs some analog signal processing. Processing features such as a gamma compensation circuit and a linear matrix circuit for obtaining "life-like" color are disabled.

Once the signal has been obtained and processed by the camera control box, it then proceeds to the Matrox Meteor card in the PC where the video frames are grabbed and digitized with an analog-to-digital converter (ADC). The ADC digitizes the signal to 8 bits which corresponds to 256 discrete counts. The way in which the signal can be digitized can be modified by black and white level inputs to the ADC from the system software.

The acquisition software makes use of the Matrox Imaging Library routines. Digital interlaced images can be obtained at the standard video rate of 30 frames per second with a spatial resolution of 640 by 480 pixels. The system can be put into a live video mode with a pseudo-color color lookup table to set up the UV lighting on the models.

Tunnel Tests

In order to set up for a wind tunnel run, the first task after mounting a model is to set up the UV lighting. The model is injected into the tunnel and a monitor is set next to the test section which displays a live pseudo-color image of the green component from the

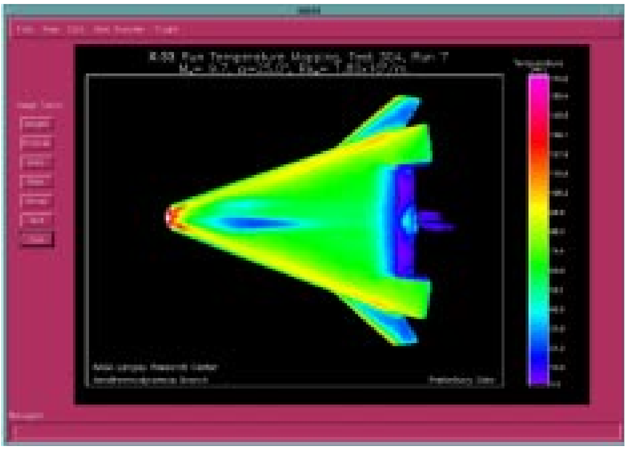

Fig. 4 Typical IHEAT interface window.

video camera. The lighting is set so that the fluorescence intensity from the model does not go over the scale limits of the phosphor system. This process is performed on the green component because this component decreases throughout a run and ultimately quenches out if a high enough temperature is reached. By keeping the green fluorescence intensity as high as possible without going overscale, temperature range and resolution is optimized.

Once the lighting is set, the model is retracted and is ready for the tunnel run. The acquisition system is set to acquire images at different times into the run. Due to possible conduction effects, earlier images provide data on high-heating, high-curvature portions of the model and later images provide data for low-heating, low-curvature portions of the model. After the acquisition system and tunnel are ready to run, the model is briefly injected into the tunnel test section and a pre-run image is obtained of the initial temperature distribution on the model. The model is retracted and the tunnel is brought up to the desired reservoir pressure and temperature conditions. The model is then injected, the acquisition system is triggered and images are acquired at the preset times. Once the run has been completed, the images are saved and ported over to a UNIX-based workstation for data reduction and analysis.

Phosphor Calibration, Data Reduction and Analysis

IHEAT

The IHEAT software package is a UNIX-based, “user-friendly” software suite of eight programs for efficiently handling the large amounts of image data associated with the phosphor thermography calibration, data reduction and data analysis. A typical IHEAT main window, shown in Fig. 4, contains an image area, a menu bar at the top and a set of tool buttons along the left side. The menu bar includes menu buttons for loading in files, working with image titles, color bar ranges, color tables, data processing and more. All processes in IHEAT are performed using the metric system, but a menu button exists for displaying results in English units. A set of tool buttons on the left side includes three options for extracting data from the IHEAT images with line cuts, a statistical tool for analyzing regions of interest in an image, a zoom feature, a button to mask over spurious data in an image and two buttons for arrow and text annotation.

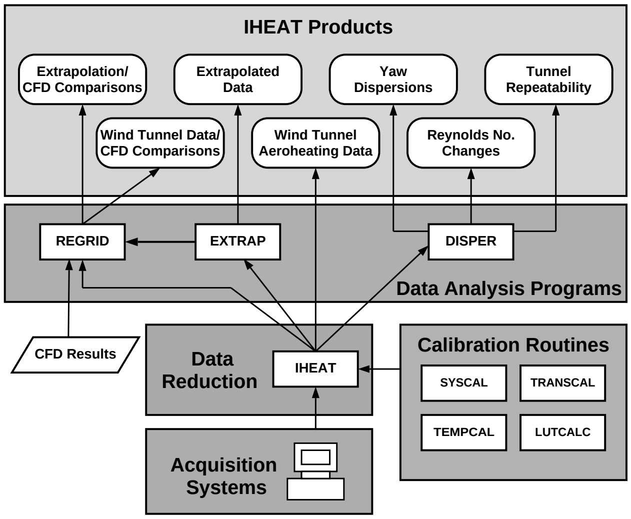

Fig. 5 The IHEAT software environment.

Figure 5 shows a schematic of the IHEAT software environment. Calibration or wind tunnel image data are acquired by the acquisition systems and sent to the calibration programs or the main data reduction program. Three calibration programs, SYSCAL, TRANSCAL, and TEMPCAL are used for reducing calibration data and the LUTCALC program packages the calibration results into temperature lookup tables for use by the IHEAT data reduction program. Once the phosphor data has been reduced, three programs exist for use in further analyzing the results. The DISPER program overlays images from different runs and provides ratios of heating between runs. EXTRAP uses the extrapolation theory previously described to determine laminar and turbulent heating levels at a point on a trajectory. The REGRID program is an interpolation program where CFD surface data can be packaged together with phosphor mappings to make direct comparisons in the global characteristics between the computations and the wind tunnel data.

Calibration

The phosphor thermography method has been developed to support work in a number of hypersonic facilities. In addition, four acquisition systems have been constructed for utilization in the facilities. The ideal situation would be a calibration process for one system, at one facility and for one phosphor mix. However with the number of systems involved, with the way acquisition systems can be shuttled between facilities and with the batch-to-batch variations which

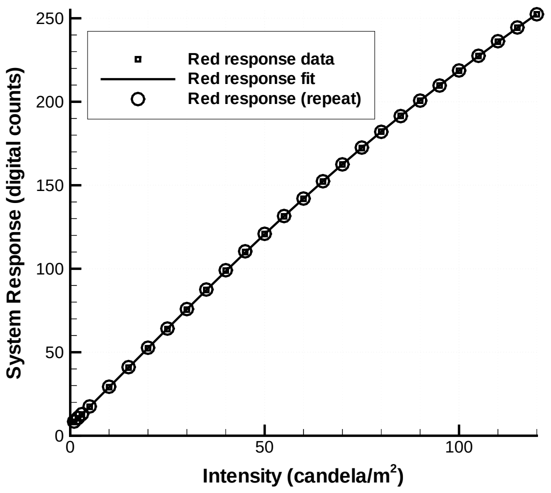

Fig. 6 Red component system calibration.

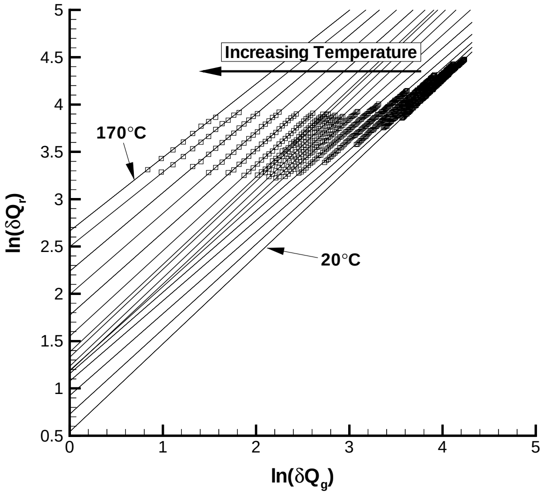

Fig. 7 Sweep of log-log lines.

can occur with the phosphors, the matrix of required calibrations can rapidly expand.

In order to reduce the number of calibrations which are required, a modular approach has been developed. Each system is calibrated individually for system response, each facility window is calibrated for transmissivity in the red and green portions of the spectrum, and the temperature/intensity response characteristics for each phosphor batch are separately calibrated. All of the calibrations are finally packaged together for any given combination via a lookup table creation program.

The first calibration required is to determine the response of the system to a given input of light, δQ, for use in Equation 9. To perform this, an acquisition system is pointed at an integrating sphere that is stepped through different intensity levels. Images are acquired at each level. In reducing the calibration data, the SYSCAL program is used. A region of interest is picked for the range of images and analyzed. From this analysis, a fourth-order fit is made for each color component of digital system response in counts versus light intensity. A sample red component calibration, along with the fit and a repeat run, is shown in Figure 6.

In characterizing the facility window transmissivities, an integrating sphere is placed behind a window at an angle relative to the window. On the other side of the window, a camera is set up and images are acquired of the integrating sphere port, with and without the window between the port and the camera. Red component and green component images are brought into the TRANSCAL program and converted to light intensity mappings and the resulting mappings are averaged to yield window transmissivity factors in both the red and green portions of the spectrum.

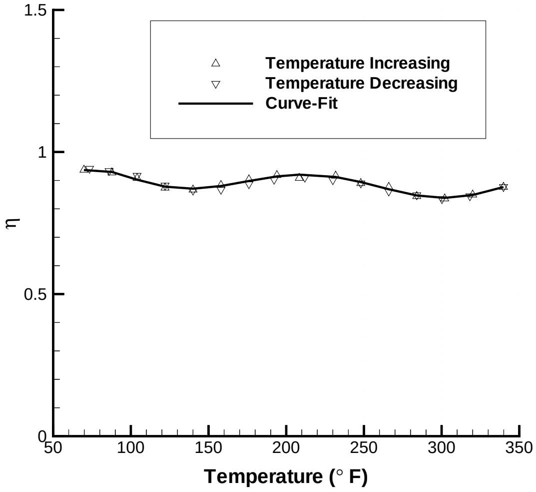

Fig. 8 Ratios of fluorescent exponents.

The final calibration determines the fluorescence response characteristics of the phosphors at different temperatures. In performing this calibration, a thin 3-inch square plate coated with phosphors is placed into a computerized convection oven which has a window on the front. The plate is illuminated with a UV lamp from outside the oven with a range of incident intensities. During a calibration the plate is viewed with an acquisition system and images are acquired at temperatures ranging from 70 to 340 $°F$. After the data is acquired, the images are analyzed with the TEMPCAL program. At each temperature, $\log(\delta Q_r)$-$\log(\delta Q_g)$ lines are determined with slopes of $\eta(T)$ and y-intercepts of $\Delta(T)$ as described by Equation 9. A sample sweep of lines from a calibration is shown in Figure 7. Once the slopes and intercepts have been determined, they are plotted versus temperature as shown in Figures 8 and 9.

Lookup tables are created from the calibrations for

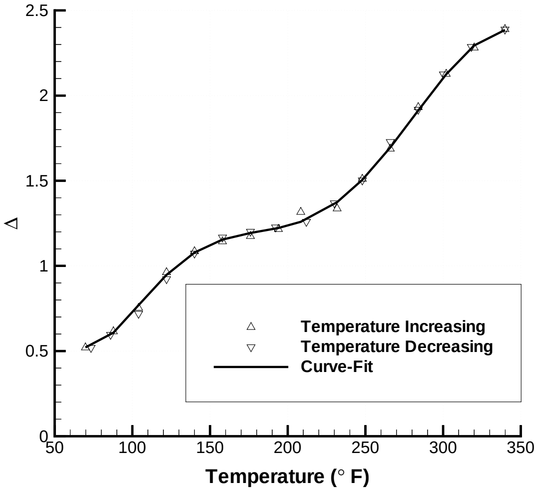

Fig. 9 Logarithmic differences.

use in IHEAT by running the LUTCALC program. When using LUTCALC, variables are set corresponding to a desired combination of the three calibrations and LUTCALC iterates on each of the possible red and green acquisition readings, ultimately creating a 256 by 256 temperature lookup array file.

Data Reduction

Data reduction is performed in the IHEAT program. When reducing the data, a setup file is first loaded into IHEAT which contains all of the specific information for the test setup including phosphor system used, facility that the test is being performed in, and the phosphor mix which has been applied to the models. Once the setup file has been loaded, a file with the tunnel flow conditions for the run being analyzed is input. This file includes the tunnel total temperature, model angle of attack and a predicted stagnation point heating value which IHEAT uses to non-dimensionalize the data. Next, the position history of the model is input and analyzed to precisely determine the effective time at which the images are to be reduced. The pre-run intensity images and run intensity images are input into IHEAT and immediately converted to temperature mappings.

Once the files have been loaded, the next step is to compute heat transfer coefficients. If a global adiabatic wall temperature is desired other than the tunnel total temperature, a menu buttion exists which allows for the calculation of the adiabatic wall temperature on a wedge with a half angle corresponding to the model angle of attack using Equation 25. At this point, the global adiabatic wall temperature is known, along with the effective time and the model run and pre-run temperatures. Equation 19 is solved at every point on the model which is in the field of view of the camera.

After the heat transfer mappings have been computed, often line cuts from the image are desired. An automated approach exists in IHEAT to do this. Desired axial and longitudinal cut locations are entered into a window in IHEAT. Next, known fiducial mark locations in the image are clicked on and also input into IHEAT. IHEAT cuts the images along the desired cut locations, stretching the cuts according to the input fiducial mark locations. Currently, the full surface geometry is not entered into IHEAT, so, more fiducial marks input into IHEAT corresponds to a greater accuracy in the locations of the cut data. Once the cuts have been obtained, they are automatically saved for comparison with cuts from other runs.

Data Analysis

IHEAT data can be extrapolated to flight surface temperature levels using the EXTRAP program. To do this, a reduced IHEAT file is entered into EXTRAP along with the desired trajectory point (described by the vehicle velocity and altitude). In addition, the predicted heat transfer coefficient at flight conditions must be input for a hemisphere of a radius scaled up from that of the hemisphere which was used to nondimensionalize the tunnel data. The type of correction for the state of the boundary layer (laminar or turbulent) must also be entered and, if it is valid, a cold-wall assumption toggle can be set to reduce computation time. Once the parameters are set, EXTRAP then calculates the surface temperature mapping at the flight conditions using Equations 30 through 36 as appropriate. After the surface temperature image has been determined, temperature line cuts can be extracted off of the image in the same way as with the tunnel data.

The second analysis program available to IHEAT is the DISPER program. Two reduced IHEAT runs are entered into this program, a baseline and some dispersion such as in yaw. The DISPER program helps the user in registering the two images over each other and then divides the dispersion run by the baseline. A number of possible uses for this analysis exist including examination of slight changes in yaw, angle of attack effects, heating augmentations on deflected flaps, Reynolds number variations, run-to-run tunnel repeatability, comparison of results between facilities and substrate conduction error estimation.

The final IHEAT analysis code is the REGRID program. REGRID is a program which converts either CFD flight surface temperature predictions or wind tunnel heat transfer rate predictions to images and puts the resulting images side by side with phosphor data. This is done by splitting the CFD surface grid computational cells into triangular elements, interpolating within each element and projecting the result back into the phosphor imaging space. The phosphor and CFD images are then displayed together along the symmetry plane of the geometry. Currently, this comparison can be performed for lee and wind views only. Since the surface geometry is available from the computational grid, the phosphor image has also been stretched in the past to account for curvature effects when not enough fiducial marks were placed on the model to adequately define a geometry.

Error Analysis

In analyzing the error for the phosphor thermography method, the AIAA standard for assessing wind tunnel data uncertainty[20] was used which in turn conforms with international guidelines and standards.[21] While a number of different uncertainty sources exist for phosphor data including those due to calibration, data acquisition and processing, lack of fidelity in the models, knowledge of the tunnel test environment, three-dimensional conduction effects within the substrate, and registration of image pixel location to physical location on the model, this analysis reports errors associated only with the first two sources (calibration and data acquisition and processing) which are the most readily quantifiable. Errors are presented with bias limits, precision limits and overall uncertainty (which is the root of the sum of the uncertainties squared). All errors are reported with 95% confidence limits. The analysis describes the uncertainty associated with each variable in Equation 19 (initial temperature, run temperature, adiabatic wall temperature, substrate thermal properties and effective time) and then presents the combined uncertainty for all of the variables.

Temperature measurement uncertainties are plotted in Figure 10. The bias error was determined from the uncertainty in the calibration oven temperature reading. The temperature distribution error through the oven test section was quoted to be 0.026 $°F$ and was considered negligible. The oven thermocouple uncertainty (furnished by the manufacturer) varied from 3.6 to 4.9 $°F$. The precision error was found by putting the temperature calibration images (which theoretically are isothermal) into IHEAT and statistically looking at the temperature measured at each pixel element, calculating a standard deviation from the nominal temperature reading in the calibration and multiplying by two for the 95% limits. From Figure 10 the temperature error varies from 5.2 to 6.5$°F$. It is seen that the precision uncertainty dominates at the lower temperature, but then the bias uncertainty dominates the overall uncertainty at temperatures higher than 140$°F$. For the combined uncertainty analysis, the error in the initial temperature was assumed to be 5.2$°F$ and the wall temperature error was assumed to be at the worst case of 6.5$°F$ through the temperature range.

In order to compute the uncertainty in the adiabatic wall enthalpy, a worst case situation was applied. The adiabatic wall enthalpy for a plate at zero degrees angle of attack was calculated and averaged with the tunnel total enthalpy. The difference between the averaged value and the tunnel total enthalpy was used as the error.

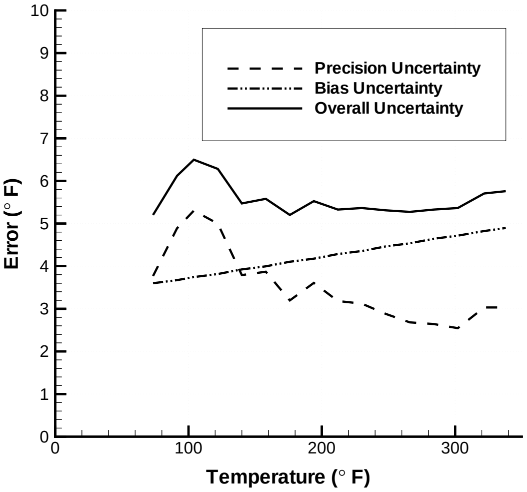

Fig. 10 Temperature errors.

For the substrate thermal properties, the quoted instrumentation uncertainty was 3% for both the diffusivity and conductivity and this was used as a bias uncertainty. A statistical analysis with a number of samples yielded precision uncertainties of 9.6% and 1.5% for diffusivity and conductivity with corresponding overall uncertainties of 10% and 3.4%. The error due to choosing an average thermal product to account for thermal properties variations (Equation 24) was previously found to be 0.4% and was assumed to be insignificant. While the diffusivity error seems large, the heat transfer rate is not ultimately as sensitive to it since a square root is taken of the diffusivity within the data reduction.

The effective time from Equation 20 was found from thin-film calibration runs to have an uncertainty of 0.055 sec. At 1 second, the error is thus 5.5%.

In determining a combined uncertainty, a standard approach is to use a first order Taylor series expansion where sensitivities of variables within an equation are found by taking the partial derivative of the equation with respect to each variable within the equation. This approach is only valid, however, when a linear function is being analyzed. The function in Equation 19 is not linear and when a first order Taylor series is used, artificially large errors arise due to the contribution of the adiabatic wall enthalpy. In order to properly compute the errors, higher order terms in the Taylor series expansion must be used. This approach became impractical, so a computer program was written where each of the variables in Equation 19 was varied by its uncertainty and the resulting heat transfer rate was compared with the heat transfer rate calculated with baseline values for the variables.

Combined uncertainties in heat transfer rate for the

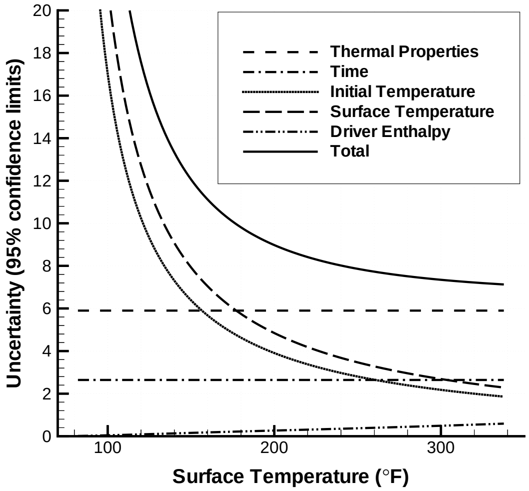

Fig. 11 Heat transfer rate errors in 31-Inch Mach 10 Tunnel.

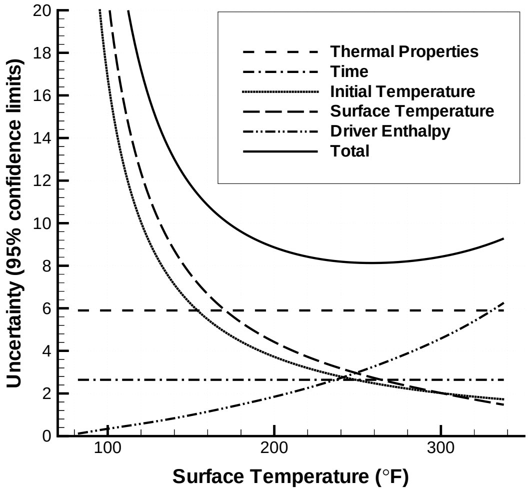

Fig. 12 Heat transfer rate errors in 20-Inch Mach 6 Tunnel.

phosphor data versus measured model surface temperature at 1 second into a run are plotted for the 31-Inch Mach 10 Tunnel and 20-Inch Mach 6 Tunnel in Figures 11 and 12 respectively. From the plots, it can be observed that the initial temperature and run temperature are the dominant uncertainties when lower surface temperatures are measured. Indeed, as the surface temperature approaches the initial temperature, the uncertainty climbs to infinity. This high error due to temperature is responsible for the large amount of scatter observed in phosphor heating data obtained from lower surface temperature readings. In most cases though, the wall temperature measurements are higher and the uncertainty due to thermal properties is the significant error source. In the case of the 20-Inch Mach 6 tunnel, at the higher end of the temperature range, the surface temperature to adiabatic wall temperature is much larger (due to the lower reservoir temperature of the tunnel) and the contribution of the error in the adiabatic wall temperature is larger than in the case of the 31-Inch Mach 10 Tunnel. For the majority of the temperature range, the resulting total phosphor uncertainty varies between 7 to 10% in the 31-Inch Mach 10 tunnel and 8 to 10% in the 20-Inch Mach 6 tunnel.

Fig. 13 Two-inch radius thin-film hemisphere.

Comparison to Thin-Film Hemisphere Measurements

A 2-inch radius phosphor hemisphere model was fabricated and tested to compare with measurements on a 2-inch radius hemisphere instrumented with thin-films. The phosphor hemisphere was made using the fabrication approach previously described. A small fiducial mark was placed at the stagnation point in order to determine the stagnation point location in the run images. In the case of the thin-film hemisphere, the model (shown in Figure 13) was made from Macor since the films could not be successfully applied to a fused slica substrate. Nine gauges were placed along an arc at two and a half degree intervals from the stagnation point back to the twenty degree location. A gauge was placed at 25 degrees and then from 30 to 70 degrees in 10-degree increments. Four additional gauges were placed in two and a half degree intervals back from the stagnation point on the other side of the model as a check on the symmetry of the measurements.

Both models were tested in the 31-Inch Mach 10 Tunnel at reservoir conditions of 720 psi and 1830°R, corresponding to a freestream Reynolds number of 1.0x$10^6/ft$. The phosphor data was reduced at time of 1 second after the model had been exposed to the flow. The thin-film measurements were reduced with a data reduction code developed by Hollis[22] which uses the Kendall-Dixon-Schulte[23] one-dimensional time history approach. All data were non-dimensionalized using the Fay-Riddell[24] stagnation point heating values calculated using the modified Newtonian method for the pressure gradient.

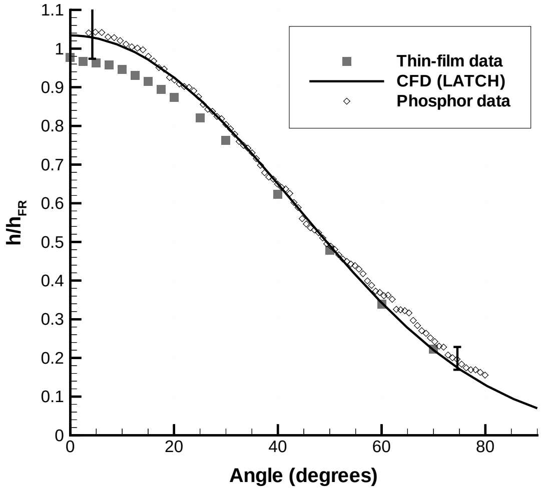

Fig. 14 Two-inch radius hemisphere phosphor/thin-film comparison.

CFD predictions were also made using the LATCH program for comparison with the wind tunnel data. LATCH uses an axisymmetric analog for three-dimensional boundary layers with boundary layer edge conditions from an inviscid flowfield solution.[25] LATCH computations for this comparison were performed, assuming equilibrium air properties, at wind tunnel conditions and non-dimensionalized in the same way as the wind tunnel data.

A cut on the phosphor image was taken from the stagnation point to the aft end of the sphere. The phosphor data from the 80 to 90 degree locations was removed due to low UV illumination which put the data out of the phosphor calibration range. Results are plotted along with the thin-film measurements and the LATCH predictions in Figure 14. Two error bars have been placed on the plot, one near the front of the sphere with an uncertainty of ±7.5% and one near the rear of the plot with an uncertainty of ±15%. The data and LATCH predictions fall within a 7 percent band through the full 80 degrees plotted in the figure. Through the first 50 degrees, however, the phosphor data tends to agree better with the CFD computations than with the thin-film data. The stagnation point heating on a hemisphere is expected to be higher than Fay-Riddell theory when the Fay-Riddell calculation is performed using the modified Newtonian method to determine the pressure gradient. This implies that the thin-film heat transfer data may be low in the stagnation point region for reasons as yet to be determined. Based on this comparison, however, the phosphor heating levels agree with thin-film measurements and computations within the uncertainties of the methods, thereby providing a degree of confidence in the phosphor technique.

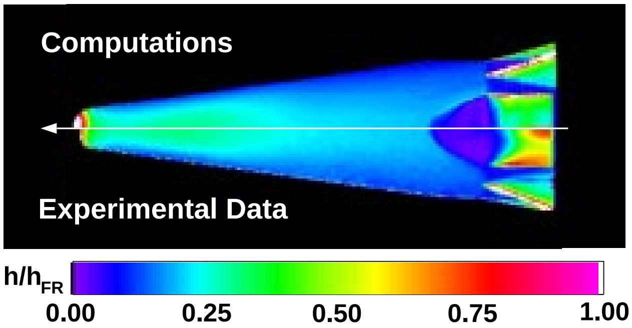

Fig. 15 VT/VL Mach 10 Phosphor/LAURA comparison, $\alpha = 17.5°$.

Computational Comparisons

Mach 10 8-Degree Sphere Cone Comparison

In support of the competitive first phase of the X-33 program, phosphor measurements were performed on a vertical takeoff/vertical lander (VT/VL) configuration and compared with CFD predictions. The VT/VL model was 12 inches long with a spherically blunted 8-degree cone forebody. The spherical nose was 1 inch in diameter. The conical forebody intersected a cylindrical aft section which had cuts taken out of it at four circumferential locations 90 degrees to each other. Flaps were located on each cut.

For this comparison, the LAURA CFD code was used for obtaining computational predictions. LAURA is an upwind-biased, point-implicit, three-dimensional, Navier-Stokes algorithm.[26] For the predictions presented here, the code was run in a laminar, perfect gas, thin-layer Navier-Stokes mode.

The VT/VL model was tested in the 31-Inch Mach 10 Tunnel at 0.0, 5.0, 17.5 and 25.0 degrees angle of attack. The data were non-dimensionalized with the stagnation point heating to a 1-inch diameter hemisphere, as calculated with the Fay-Riddell theory. CFD predictions were calculated using tunnel run conditions at each angle angle of attack. The CFD results at 17.5° angle of attack were run through the REGRID program previously described and the results are shown in Figure 15. In the figure, good agreement on the conical forebody can be observed although back on the flap (deflected at 20°), the phosphor data shows substantially higher heating. The disagreement on the flap is believed to be due to the separated free-shear layer from the cone transitioning and reattaching on the flap, a flow situation which is challenging for CFD computations to predict.

Centerline cuts were also obtained at each angle of attack on the conical forebody only and the results comparing the CFD predictions with the phosphor data are shown in Figure 16. The results at the higher angles of attack show an initial drop in heating followed by a slight rise due to the occurance of an over-expansion followed by a recompression in the nose region of the model. In general, at all angles of attack,

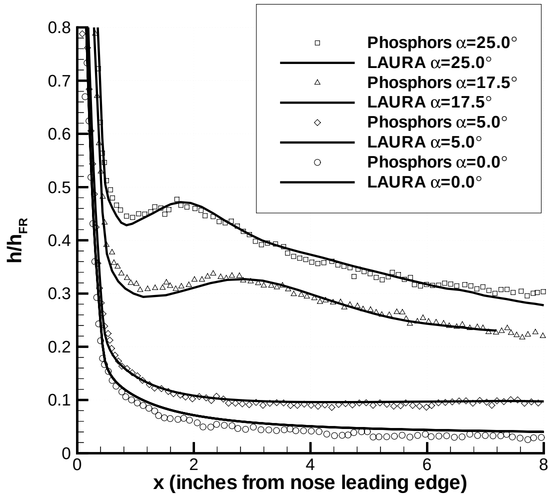

Fig. 16 VT/VL Mach 10 windward centerline heating comparison between phosphor data and LAURA computations.

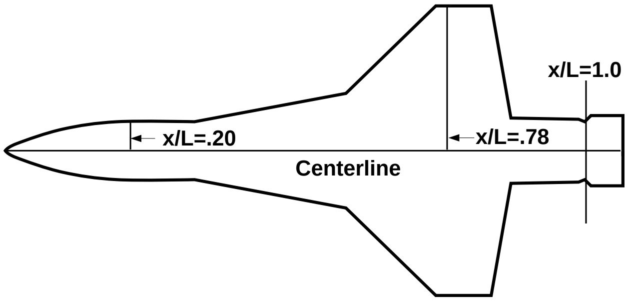

Fig. 17 X-34 planform with profile cut locations.

there is very good agreement between the phosphor data and CFD predictions.

Mach 6 X-34 Comparison

CFD comparisons have also been made on an X-34 configuration (planform shown in Figure 17) at Mach 6 conditions. For this study, 0.0183-scale phosphor models were fabricated and tested in the 20-Inch Mach 6 Tunnel at freestream Reynolds numbers varying from 0.59 to $7.95\times10^6/ft$. as described in Ref. 4.

The CFD computations were performed using LAURA, LATCH and GASP as described in Refs. 27, 28, and 4 respectively. The codes were run in laminar and turbulent perfect gas modes at tunnel conditions corresponding to a freestream Reynolds number of $7.86\times10^6/ft$. The LAURA and the GASP calculations used the same grid which was shock-adapted from the LAURA code.

REGRID comparisons between the laminar LAURA and GASP results and phosphor data are shown in Figs. 18 and 19. Turbulence results are shown in Figs. 20 and 21.

In the images, the phosphor data is seen to have a sharp jump in heating due to the onset of transition

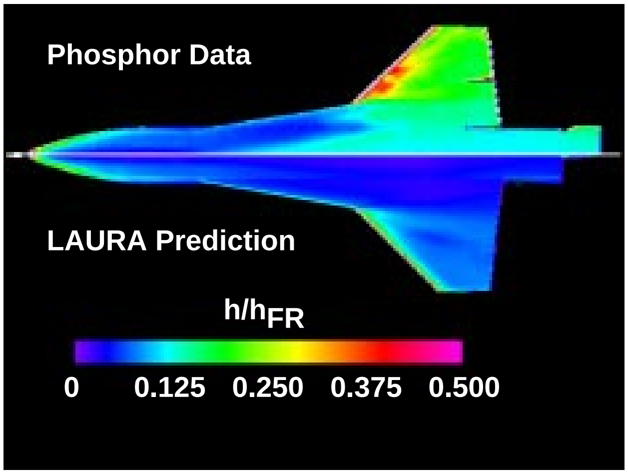

Fig. 18 Laminar Phosphor/LAURA X-34 comparison, $\alpha = 15°$.

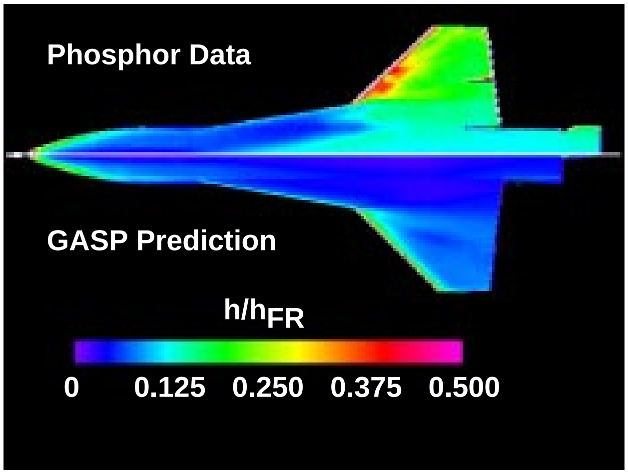

Fig. 19 Laminar Phosphor/GASP X-34 comparison, $\alpha = 15°$.

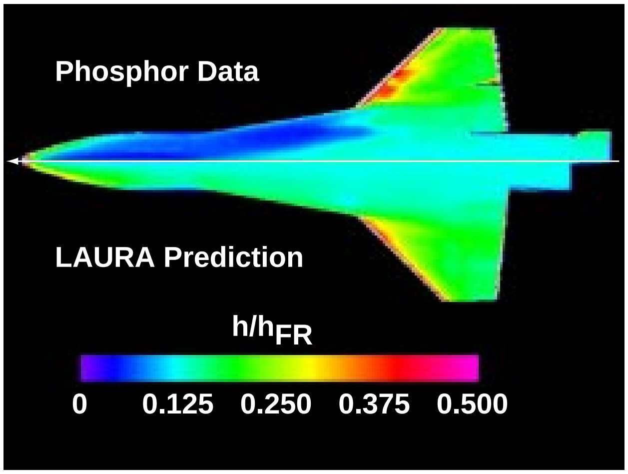

Fig. 20 Turbulent Phosphor/LAURA X-34 comparison, $\alpha = 15°$.

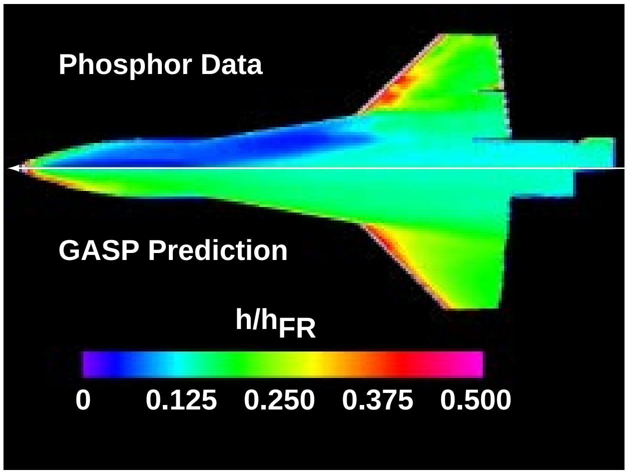

Fig. 21 Turbulent Phosphor/GASP X-34 comparison, $\alpha = 15°$.

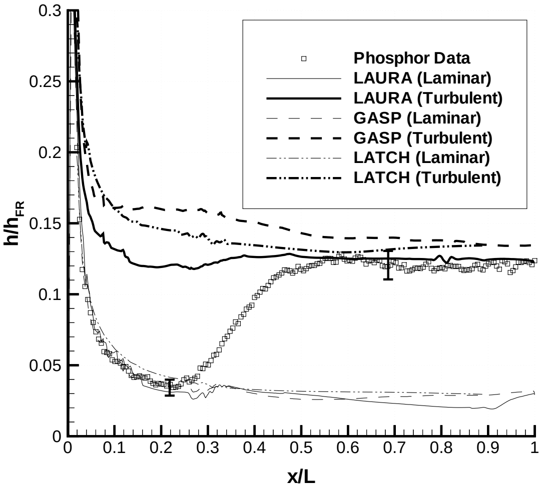

Fig. 22 Phosphor/CFD X-34 centerline comparison.

starting a third of the way back along the centerline. In comparing the phosphor data to the computational results, the laminar predictions should only be compared with the laminar phosphor data and the same is true for the turbulent predictions. The images show that the GASP predictions appear to run higher than the LAURA predictions in both the laminar and turbulent cases.

Line cuts were taken from the phosphor and CFD results along the centerline, and at axial stations (shown in Fig. 17) of x/L=0.2 and 0.78, where L is defined to be from the nose to the junction between the flap and the fuselage. The centerline phosphor heating in Fig. 22 in the nose is laminar. A minimum is seen in the heating and then the flow transitions to turbulence from an axial station of 0.25 to about 0.55. Agreement between the LAURA predictions and the phosphor data in both the laminar and turbulent regions is within experimental uncertainty. The GASP data tends to agree in the laminar region, but is higher than the phosphor results in the turbulent region. The LATCH results split the difference between the LAURA and GASP results in the turbulent region but are higher than the phosphor data and LAURA and GASP predictions in the laminar region.

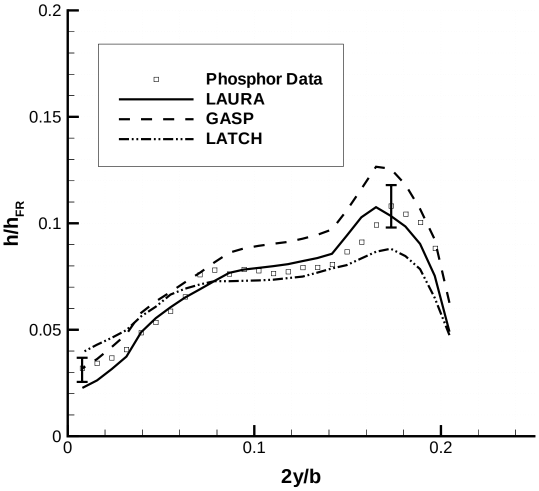

Fig. 23 Laminar phosphor/CFD X-34 comparison at x/L=0.02.

Figure 23 shows laminar comparisons at the 0.2 axial station with respect to $2y/b$ where y is the spanwise location and b is the total span from wing tip to wing tip. The LAURA predictions agree with the phosphor data to within the data uncertainty for most of the cut while the GASP predictions tend to run a little higher than the phosphor data and the other predictions. The LATCH predictions start off higher than the phosphor data near the centerline and end up low outboard on the fuselage.

In the case of the 78 percent cut, Fig. 24, accurately predicting the heating is more difficult because of the presence of the bow-shock/wing-shock interaction on the wing. The LAURA predictions are in qualitative agreement with the phosphor results. Along the cut from the centerline, the heating experiences a rise as the heating from the wing fuselage junction is reached. Part of the footprint of the shock impingement is seen by the the two lower humps in the phosphor data and the single lower hump in the LAURA prediction. Finally, a rise is seen toward the wing tip in both the phosphor and LAURA results with a slight drop in the phosphor results due to the fact that a laminar portion of the wing is being cut. Qualitatively and quantitatively, the results are not quite as good with the GASP and LATCH results. Both of these codes tended to smear out the characteristics associated with the shock interaction.

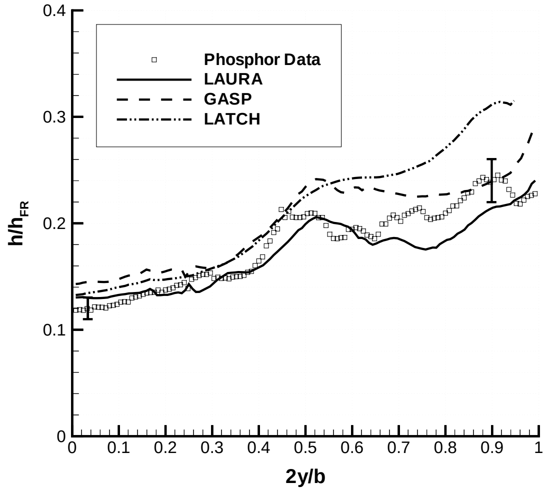

Fig. 24 Turbulent phosphor/CFD X-34 comparison at x/L=0.78.

Application of Extrapolation Analysis to the X-34

Based on the relatively good agreement between the phosphor data and the LAURA computations at tunnel conditions, the extrapolation theory previously described was applied to the X-34 phosphor data and compared to LAURA flight surface temperature predictions. Phosphor data at $\alpha = 23°$ were used, since both laminar and turbulent predictions were available at this angle of attack.

The phosphor data was extrapolated to flight surface temperatures using the EXTRAP program. Flight conditions for the comparison were at an altitude of $118{,}419 ft.$ and a velocity of $6490 ft/s$ which corresponded to Mach 6.4 and a length Reynolds number of 16.2×10^6. In the case of the laminar data, a run was used with $Re_\infty = 1.0 \times 10^6/ft.$ With the turbulent extrapolation, a Reynolds number deficit existed between the tunnel conditions and the flight conditions, so two runs were used at $Re_\infty = 4.4 \times 10^6/ft.$ and $7.8 \times 10^6/ft.$ to show the applicability of the method to different tunnel Reynolds numbers.

Laminar Extrapolation

The global comparison between the laminar phosphor data and the LAURA computations is shown in Fig. 25 along with a centerline cut and an axial cut at x/L=0.78 in Figs. 26 and 27 respectively.

Generally the surface temperature levels compare well over the whole image. On the wing, the patterns due to the shock impingement appear somewhat sharper with the phosphor data than with the CFD predictions, possibly due to lack of grid resolution on the part of the CFD computatons. On the centerline cut, the CFD curve is flatter than the phosphor curve with the phosphor results meandering on either side of the CFD predictions, the worst disagreement being about $100°F$ towards the aft end of the configuration. In the case of the axial cut, good agreement is observed with the exception of the fact that the smeared shock footprint in the CFD computation lowers the peak temperature predicted on the wing by approximately 150°.

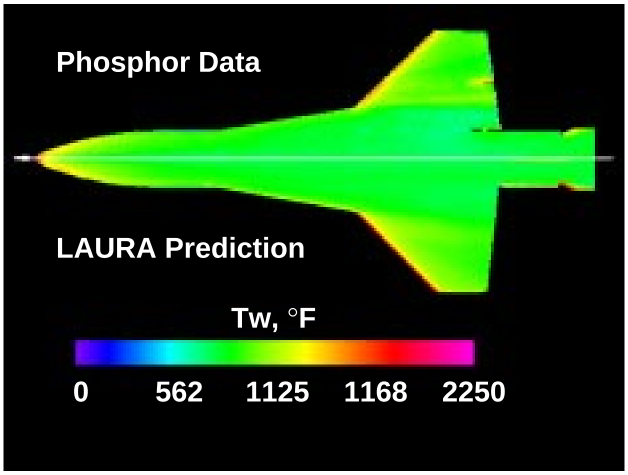

Fig. 25 Laminar surface temperatures at $\alpha = 23°$.

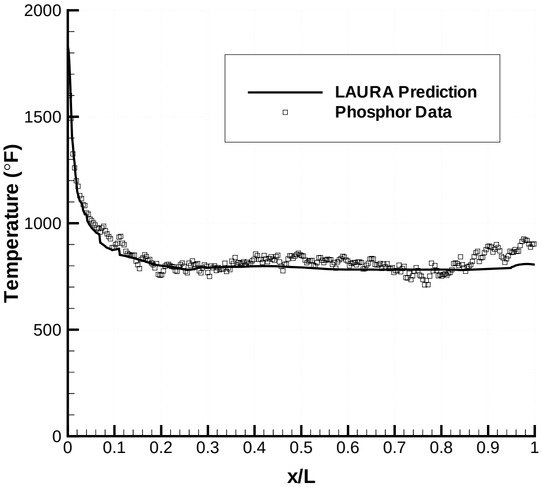

Fig. 26 Laminar centerline flight surface temperatures.

Turbulent Extrapolation

The global comparison between the turbulent phosphor data extrapolated from the $8 \times 10^6/ft.$ freestream Reynolds number case and the LAURA computations is shown in Fig. 28. The rearward part of the fuselage in the compuational results is not shown since it was not available at the time the extrapolations were performed. In the turbulent case, good agreement in the surface temperature levels is generally observed with the exception of the region outboard of the interaction region and perhaps near the wing leading edge where the phosphor data predicts slightly higher tempera-

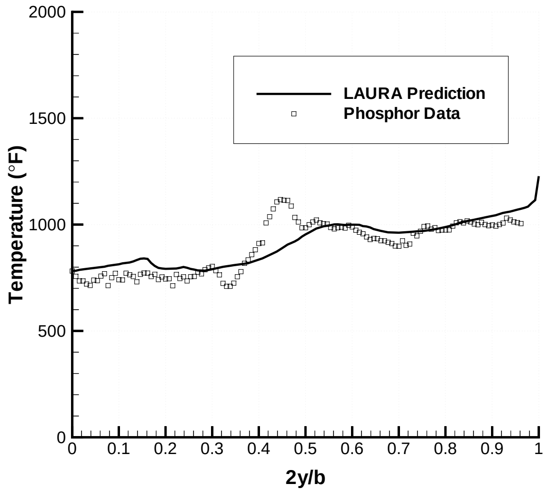

Fig. 27 Laminar flight surface temperatures at x/L=0.78.

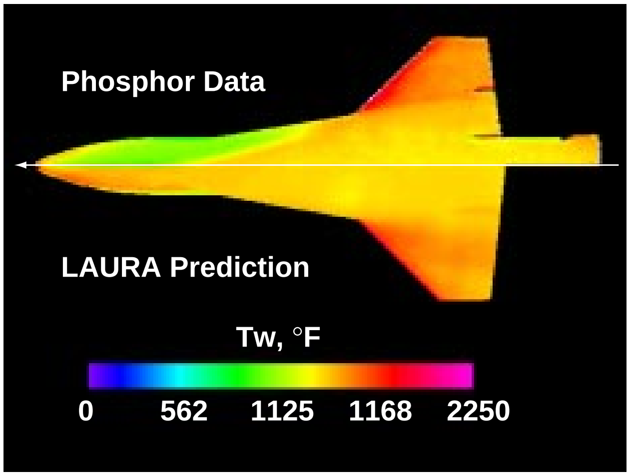

Fig. 28 Turbulent surface temperatures at $\alpha = 23°$.

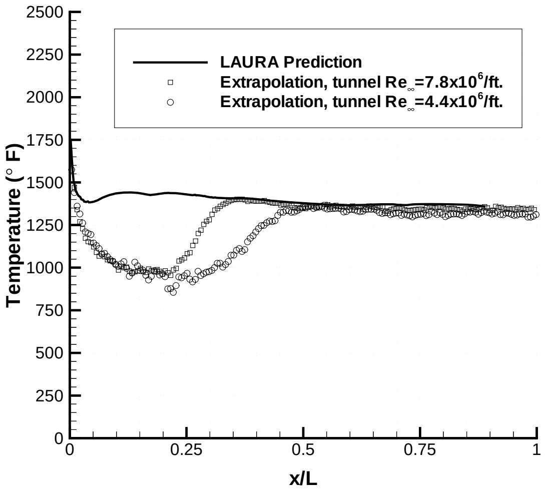

Fig. 29 Turbulent centerline flight surface temperatures at $\alpha = 23°$.

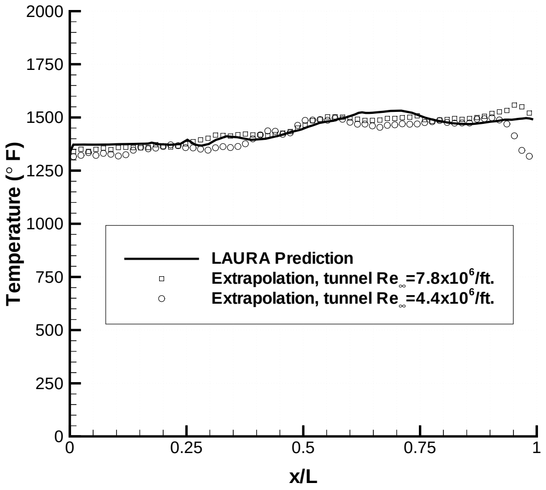

Fig. 30 Turbulent flight surface temperatures at x/L=0.78.

tures. Line cuts are shown on the centerline and at an axial station of x/L=0.78 in Figs. 29 and 30 respectively. For the phosphor data, extrapolated results are shown from two runs, at $Re_\infty = 4.4 \times 10^6/ft.$ and $7.8 \times 10^6/ft.$ Agreement is seen to within $75°F$ everywhere in the two plots where laminar flow exits on the wind tunnel model.

As previously stated, the purpose in using extrapolated data from tunnel runs at two different freestream Reynolds numbers was to show the versatility of the extrapolation theory, in spite of a Reynolds number deficit between the tunnel and the flight conditions. Figure 31, which shows centerline cuts of unextrapolated wind tunnel data at $Re_\infty = 4.4 \times 10^6/ft.$ and $7.8 \times 10^6/ft.$, is presented to illustrate the fact there is a significant difference (as much as 30 percent) in the heat transfer levels in the turbulent region between the two Reynolds number conditions. Without the turbulent extrapolation factor previously derived, this would correspond to over a $120°F$ difference in predicted flight surface temperature levels. This difference is not observed on the centerline cut between the two Reynolds number runs.

Concluding Remarks

This paper has presented the basic process which is used at the Langley Research Center in obtaining phosphor thermography data in hypersonic facilities. A new weighted relative-intensity fluorescence theory allows for the quantitative determination of surface temperature measurements on complex models having large of suface curvature. Application of an enthalpy-based approach to solving the heat conduction equations along with calibration of the effective starting

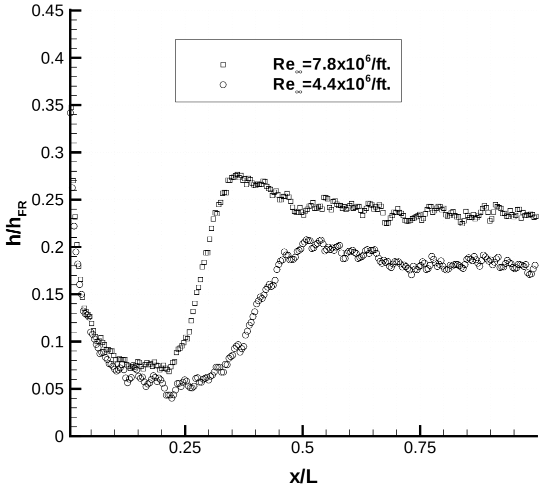

Fig. 31 Tunnel centerline heat transfer coefficients at Re_∞ =4.4 and 7.8x10^6/ft.

time of a run and a simple approach for accounting for variable substrate thermal properties improves the accuracy of global heat transfer computations. In addition, a method has been developed for extrapolating wind tunnel data to flight surface temperatures. A user-friendly set of GUI-driven codes, collectively known as IHEAT, allows for the rapid reduction and analysis of the large amount of image data associated with phosphor thermography. Coupled with this process is a rapid ceramic model casting technique. The result is a methodology which quickly provides a wealth of information critical to the design of a thermal protection system including effects of Reynolds number, Mach number, angle of attack, control surface deflection and sideslip angle.

Acknowledgements

The following people are gratefully acknowledged for their contributions to this work: Chris Riley for his LAURA VT/VL centerline solutions; Scott Berry and Tom Horvath for the X-34 phosphor data; Bill Wood and Chris Glass for the 15-degree laminar and turbulent X-34 LAURA and GASP solutions, respectively; and Bill Kleb for the laminar and turbulent 23-degree flight solutions.

References

[1] Berry, S. A., Bouslog, S. A., Brauckmann, G. J., and Caram, J. M., "Boundary Layer Transition Due to Isolated Roughness: Shuttle Results From the LaRC 20-Inch Mach 6 Tunnel," AIAA Paper 97–0273, Jan. 1997.

[2] Thompson, R., Hamilton, H., Berry, S., T.J.Horvath, and Nowak, R., "Hypersonic Boundary-Layer Transition for X-33 Phase II Vehicle," AIAA Paper 98–0867, Jan. 1998.

[3] Hamilton, H. H., Weilmuenster, K. J., Horvath, T. J., and Berry, S. A., "Computational/Experimental Aeroheating Predictions for X-33 Phase II Vehicle," AIAA Paper 98–0869, Jan. 1998.

[4] Berry, S. A., Horvath, T. J., DiFulvio, M., Glass, C. E., and Merski, N. R., "X-34 Experimental Aeroheating at Mach 6 and 10," AIAA Paper 98–0881, Jan. 1998.

[5] Campbell, C. H., Caram, J. M., Berry, S. A., Horvath, T. J., and Merski, N. R., "An Overview of X-38 Hypersonic Aerothermodynamic Wind Tunnel Data and Comparison with Numerical Results," AIAA Paper 97–2475, Jun. 1997.

[6] Berry, S. A., Horvath, T. J., and Williams, G. B., "Results of Aerothermodynamic and Boundary Layer Transition Testing of 0.0362-Scale X-38 (Rev 3.1) Vehicle in NASA Langley 20-Inch Mach 6 Tunnel," NASA TM 112857, Sep. 1997.

[7] Loomis, M. P., Venkatapathy, E., Papadopoulos, P., Davis, C. B., Campbell, C., Berry, S. A., Horvath, T. J., and Merski, N. R., "Aerothermal CFD Validation and Prediction for the X-38 Program," AIAA Paper 97–2484, Jun. 1997.

[8] Buck, G. M., "An Imaging System for Quantitative Surface Temperature Mapping Using Two-Color Thermographic Phosphors," ISA Paper 88–0772, May 1988.

[9] Buck, G. M., "Surface Temperature/Heat Transfer Measurement Using a Quantitative Phosphor Thermography System," AIAA Paper 91–0064, Jan. 1991.

[10] Merski, N. R., "A Relative-Intensity Two-Color Phosphor Thermography System," NASA TM 104123, Sep. 1991.

[11] Merski, N. R., "An Improved Two-Color Relative-Intensity Phosphor Thermography Method For Hypersonic Wind Tunnel Aeroheating Measurements," Dsc dissertation, 1998.

[12] Garlick, G., *Luminescent Materials*, Clarendon Press, Oxford, 1949.

[13] Thomas, A. C. and Perlbachs, A. P., "Application of Ground Test Data to Reentry Vehicle Design," Tech. Rep. AFFDL-TR-66-229, Air Force Flight Dynamics Laboratory, Jan. 1967.

[14] Tauber, M. E. and Meneses, G. P., "Aerothermodynamics of Transatmospheric Vehicles," AIAA Paper 86–1257, Jun. 1986.

[15] Anderson, J. D., *Hypersonic and High Temperature Gas Dynamics*, McGraw-Hill Book Company, 1989.

[16] McBride, B. J., Gordon, S., and Reno, M. A., "Coefficients for Calculating Thermodynamic and Transport Properties of Individual Species," NASA TM 4513, Oct. 1993.

[17] *U.S. Standard Atmosphere*, National Oceanic and Atmospheric Administration, NASA and U.S. Air Force, Washington, DC, 1976.

[18] Buck, G. M. and Vasquez, P., "An Investment Ceramic Slip-Casting Technique for Net-Form, Precision, Detailed Casting of Ceramic Models," U.S. Patent 5,266,252, Nov. 1989.

[19] Micol, J. R., "Langley Aerothermodynamic Facilities Complex: Enhancements and Testing Capabilities," AIAA Paper 98–0147, Jan. 1998.

[20] *AIAA Standard: Assessment of Wind Tunnel Data Uncertainty*, American Institute of Aeronautics and Astronautics, Washington, D.C., AIAA Standard No. S-071-1995, 1995.

[21] *Guide to the Expression of Uncertainty in Measurement*, International Organization for Standardization, Switzerland, Corrected Edition, ISBN 92-67-10188-9, 1995.

[22] Hollis, B. R., "User's Manual for the One-Dimensional Hypersonic Experimental Aero-Thermodynamic (1DHEAT) Data Reduction Code," NASA CR 4691, Aug. 1995.

[23] Kendall, D. N., Dixon, W. P., and Schulte, E. H., "Semiconductor Surface Thermocouples for Determining Heat-Transfer Rates," *IEEE Transactions on Aerospace and Electronic Systems*, Vol. 3, No. 4, Jul. 1967, pp. 596–603.

[24] Fay, J. A. and Riddell, F. R., "Theory of Stagnation Point Heat Transfer in Dissociated Air," *Journal of Aeronautical Sciences*, Feb. 1958, pp. 73–85.

[25] Hamilton, H. H., Greene, F. A., and DeJarnette, F. R., "An Approximate Method for Calculating Heating Rates on Three-Dimensional Vehicles," AIAA Paper 93–2881, Jul. 1993.

[26] Gnoffo, P. A., "An Upwind-Biased, Point-Implicit Relaxation Algorithm for Viscous, Compressible Perfect-Gas Flows," Tech. Rep. TP-2953, NASA, Feb. 1990.

[27] Kleb, W. L., Wood, W. A., Gnoffo, P. A., and Alter, S. J., "Computational Aeroheating Predictions for X-34," AIAA Paper 98–00879, Jan. 1998.

[28] Riley, C. J., Kleb, W. L., and Alter, S. J., "Aeroheating Predictions for X-34 Using an Inviscid-Boundary Layer Method," AIAA Paper 98–00880, Jan. 1998.